Structural colors based on diamond metasurface for information encryption

Jiteng Gu, Yan Liu, Nannan Meng, Vicknesh Sahmuganathan, Sze Chieh Tan, John Sudijono, Jiecong Tang, Eswaranand Venkatasubramanian, Abhijit Mallick, Febiana Tjiptoharson, Soroosh Daqiqeh Rezaei, Siew Lang Teo, Qiang Zhu, Yunjie Chen, Ming Lin*, Zhaogang Dong*, Kian Ping Loh*

Jiteng Gu, Nannan Meng, Kian Ping Loh
Department of Chemistry, National University of Singapore
117543, Singapore
Email: *chmlohkp@nus.edu.sg (K. Loh)*

Vicknesh Sahmuganathan, Sze Chieh Tan, John Sudijono, Jiecong Tang, Eswaranand Venkatasubramanian, Abhijit Mallick
Applied Materials - NUS Advanced Materials Corporate Lab, Singapore
117548, Singapore

Soroosh Daqiqeh Rezaei
Pennsylvania State University

Yan Liu, Febiana Tjiptoharson, Siew Lang Teo, Qiang Zhu, Yunjie Chen, Ming Lin, Zhaogang Dong
Institute of Materials Research and Engineering (IMRE), Agency of Science, Technology, and Research (A*STAR), 2 Fusionopolis Way, #08-03, Innovis
138634, Singapore
Email: *m-lin@imre.a-star.edu.sg (M. Lin)*; *dongz@imre.a-star.edu.sg (Z. Dong)*

Author Contributions

# J. Gu and Y. Liu contributed equally to this work.

ABSTRACT Structural colors based on dielectric metasurfaces are attractive because of their potential application in next-generation optically variable devices for anti-counterfeiting. However, the commonly used dielectric materials suffer from the issues of high light absorption (e.g., Si at blue wavelength) and low resistance to corrosion (e.g., titanium oxide), which greatly limit their application as structural color for information encryption. Here, we demonstrate the nanostructured diamond metasurface structural color constructed on nanocrystalline diamond (NCD) film by using bias enhanced nucleation (BEN) technique. Owing to the formation of highly crystalline diamond by the BEN process, the synthesized NCD film with a thickness of ~ 500 nm exhibits excellent optical quality with a relatively high refractive index that produces a strong magnetic dipole mode by Mie resonance. To realize the dynamic functionalities of diamond metasurface color with high resolution, a periodic array of asymmetric diamond cuboids with high aspect ratio (~ 3.1) was fabricated, which produces polarization-dependent response due to the enhanced Mie resonance. By optimizing the configuration of the diamond-metasurface system, the color performance was improved with high brightness and a relative wide gamut (~ 65 % of the sRGB). Our work demonstrates for the first time that NCD can serve as a robust and highly tunable dielectric platform for application in information encryption.

KEYWORDS

Structural color; Encryption information; Diamond metasurface; Mie resonance; Polarization-dependent response

1 Introduction

Structural color based on microscopic surface structure has been extensively studied due to the merits of good color saturation [1], excellent durability [2] and long-term stability [3], which are highly promising for applications in dynamic color printing [4], secure encryption and digital display [5]. A prominent example of structural colors is the plasmonic color resulting from the localized surface plasma resonance on metal nanomaterials, which can cover the entire visible spectrum and generate vivid images [6-8]. However, the high absorption and severe intrinsic losses from metallic components in resonant plasmonic system greatly limit the color saturation. Alternatively, dielectric materials like silicon and titanium oxide have demonstrated great potentials in achieving structural colors with high resolution and wide gamut. Compared with plasmonic resonance, both electric and magnetic dipole modes are supported on the subwavelength unit cells of the dielectric metasurface due to the occurrence of Mie scattering [9]. Possessing a high refractive index is a prerequisite of these dielectric materials for effectively controlling the reflection or transmission spectrum to get pure and bright colors. However, conventional dielectric materials are disadvantaged by high light absorption at blue wavelength regime (e.g., polycrystalline and amorphous silicon) [10-12] and low resistance to corrosion (e.g., titanium dioxide) [13]. Thus, developing a robust dielectric material with low-loss, high refractive index and good durability is highly demanded for application in metasurface colors.

Diamond can be a perfect candidate for realizing the dielectric metasurface colors owing to its outstanding physical and chemical properties. Diamond possesses a high refractive index (~ 2.4 @ $633\ \mathrm{nm}$) and negligible extinction coefficient in the visible spectrum range [14]. Its inertness to extreme pH and good oxidation stability in air make it highly durable. Diamond also has a high thermal conductivity and an ultrawide transparent window from mid-wave UV to IR range [15]. Consequently, diamond-based optics, such as optical waveguides [16], resonators [17] and metalens [18], have been widely used. In addition, a recent theoretical study predicted that the performance of diamond metasurface is comparable to that of all-dielectric TiO_2 metasurfaces [19]. By tuning the geometric dimensions of diamond metasurfaces, the simulated structural color exhibits a broader gamut and higher saturation than that of metallic metasurface [20].

Although polycrystalline diamond film over large area $20 \times 30\ \mathrm{cm}^2$ can be grown at low temperature (≈ 250 ℃) in $CH_4/CO_2/H_2$ plasma [21], the traditional wet "seeding" step performed

on silicon substrate before diamond film deposition is time consuming and the nanodiamond particles used for seeding are also costly, resulting in the substantial increase of the fabricating cost. To form optical NCD film on silicon substrate without the interfering effect of the seeding diamond particle layer, it is desirable to bypass the wet seeding method. A bias enhanced nucleation (BEN) method has been proposed during which an external electric field is created to accelerate the bombardments of charged carbonaceous species on substrate surface, producing a sub-surface implanted sp^3-rich layer for seeding diamond growth [22-24].

Here, we report the growth of NCD film on silicon substrate by BEN technique at 500 ℃ in $CH_4/H_2/CO_2$ gases. Our deposition temperature is substantially lower than previously reported BEN process [25-28], on account of the linear antenna plasma used [29, 30]. We found that controlling the plasma chemistry during BEN process enables the optical properties of the NCD films to be tuned. Lithographically patterning asymmetric diamond cuboid unit with a high aspect ratio (~ 3.1), enables polarization-dependent response to be engineered, leading to dynamic colors with high resolution. The presence of Si_3N_4 layer beneath the diamond cuboid improves the coloration performance with a relatively wide gamut (65 % of sRGB) and high color brightness. Our work demonstrates that highly tunable structural colors based on Mie-resonant diamond metasurface is potentially useful for generating encrypted patterns with long-durability and high-resolution.

2 Experimental Section

2.1 NCD film deposition

A customized 2.45 GHz linear antenna microwave plasma (LAMP) system was employed to deposit nanocrystalline diamond (NCD) film. Prior to deposition, p-type silicon or silicon nitride coupon ($30 \times 30\ mm^2$) was firstly cleaned in Ar/H_2 plasma for 5 min and then a negative bias voltage (− 100 V) was applied to Mo plate to promote the formation of diamond nuclei in rich CH_4 gas atmosphere. The duration of bias voltage lasted for 30 min. After the bias enhanced nucleation (BEN) process, the methane content was reduced to 4 % for depositing continuous diamond films. Details of BEN process and NCD film growth are shown in Table S1 in Supporting Information.

2.2 Sample Fabrication

NCD film with thickness of ~ 500 nm was grown on silicon substrate, and diamond cuboid array

was fabricated by electron-beam lithography (EBL) and plasma etching techniques. A 100 nm thick hydrogen silsesquioxane (HSQ) photoresist (PR) (Dow Corning, XR-1541-006, 6% dissolved in methyl isobutyl ketone) was spin-coated on NCD film surface and then EBL technique was used to print target patterns on the PR layer. After development (NaOH/NaCl solution) step, the sample was selectively etched in Cl_2/O_2 plasma in ICP-RIE tool. Finally, the residual HSQ later was wet chemically removed away in hydrofluoric acid solution.

2.3 Sample Characterization

A Raman microscope spectroscope equipped with 325 nm laser source (Power output 25 mW) was used to assess the quality of diamond films. The optical properties of NCD film was assessed by a variable angle spectroscopic ellipsometer (J. A. Woollam). The measurement was performed using three different incidence angles (50°, 55°, 60°) and ellipsometry fitting was done by applying a four-phase optical model [31-33]. The optical reflectance spectra were acquired by using a CRAIC micro-spectrophotometer QDI 2010 (Zeiss) The optical microscope image of color pallet was taken in microscope (Olympus MX61) equipped with "analySIS" software. More details about sample characterizations are provided in Supporting Information.

2.4 Theoretical Simulations

A commercial software (Lumerical FDTD Solutions) was used to calculate the electromagnetic filed distribution and optical spectrum based on the finite-difference time-domain (FDTD) method. From the top view of the nanocuboid, along X-/Y- direction, periodic boundary conditions were employed to mimic the periodic arrangement of nanocuboid unit. The perfectly matched layer serving as absorbing layer for outgoing wave was also applied in the transmission and reflection direction (Z-direction). The contributions of electric dipole and magnetic dipole resonances were analyzed with multipolar decomposition. The CIE 1931 chromaticity diagram was calculated by the color matching functions according to experimental reflectance spectrum [1].

3 Results and Discussion

Diamond cuboid array was fabricated on as-grown NCD films by electron-beam lithography (EBL) and plasma etching. The fabrication procedure is schematically illustrated in Fig. 1a. Figure 1b shows the schematic of diamond metasurface consisting of diamond cuboid unit cells on an ultra-thin nanocrystalline diamond (UNCD) film layer. The length and width of patterned cuboid are

denoted as L_x and L_y, and the distance between the adjacent units is denoted as g_x and g_y, respectively. By controlling the duration of the plasma etching process, the height of unit cell was fixed at ~ 450 nm and beneath it, a ~ 50 nm thick UNCD film served as the anti-reflection coating for the substrate. As shown in Fig. 1c, symmetric ($L_x = L_y$) and asymmetric diamond cuboids ($L_x \neq L_y$) can be lithographically patterned on NCD/Si substrate. To enable polarization-dependent response and dynamic colors, asymmetric diamond cuboids with a constant ratio of side length ($L_x/L_y \approx 3.1$) were fabricated. A multiple-colors palette based on diamond metasurface was also developed on NCD/Si_3N_4/Si substrate by simultaneously varying side length L (L_x, L_y) and gap size g (g_x, g_y) to expand color gamut and enhance color saturation.

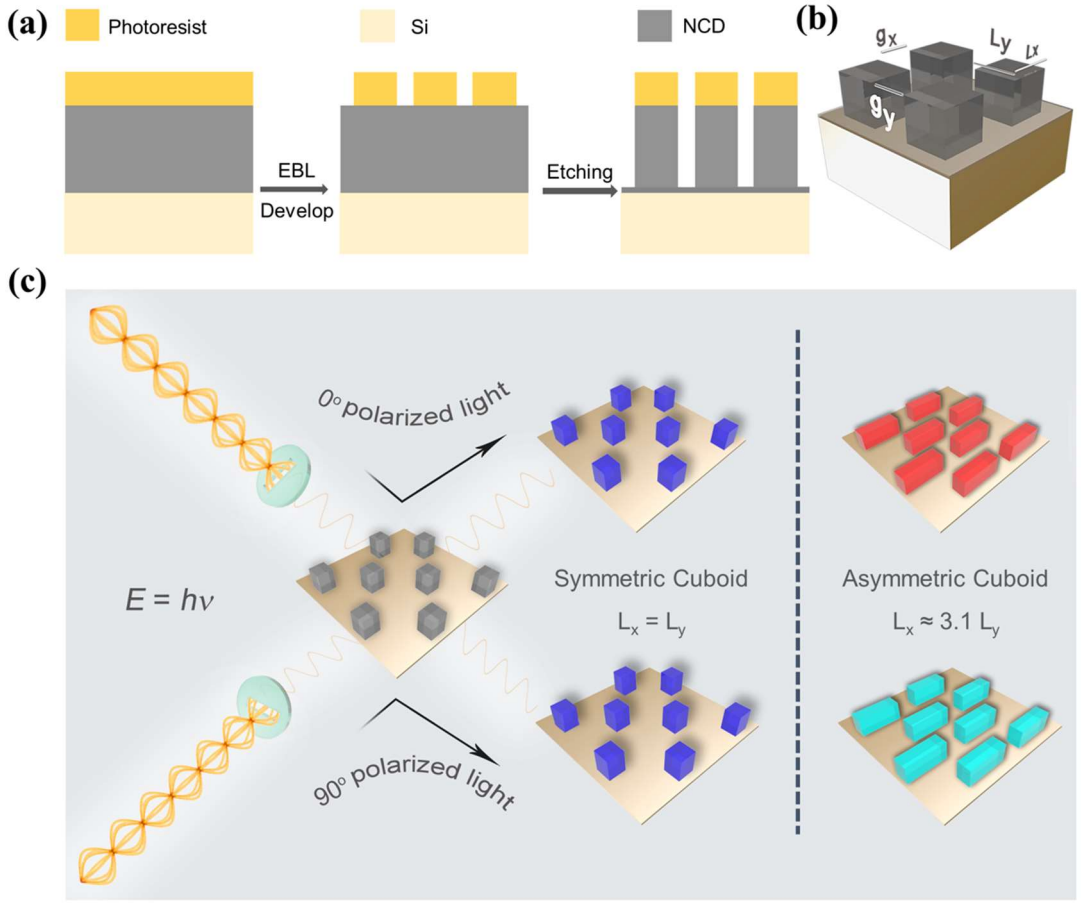

Fig. 1 Structural color metasurface fabricated on diamond cuboid nanostructures. **a** The fabrication procedure and **b** geometric configuration of the designed diamond metasurface. The diamond metasurface consists of cuboid array and UNCD film layer on silicon substrate. The height of each unit cell is fixed at ~ 450 nm. A ~ 50 nm thick UNCD film is at the interface between diamond cuboid and silicon substrate, serving as a self-anti-reflection layer. **c** The schematic of structural color produced on diamond metasurface under X- (0°) and Y- (90°) polarized light. Polarization-

dependent response and dynamic colors are realized on these asymmetric diamond cuboids.

To form optical quality NCD film on silicon substrate, the BEN process was used for directly seeding diamond growth. As shown in Fig. 2a and Fig. S1a-b, a high density of diamond nuclei ($\sim 10^{11}$ cm^{-2}) is achieved by performing BEN pretreatment using 20% CH_4 gas mixture at constant bias voltage of -100 V for 30 min. To grow NCD film possessing properties of high refractive index and high transparency, we investigated the optical properties of the film as a function of CH_4 concentration in gas mixture during the BEN process. The concentration and type of radical species were monitored by in-situ OES in Fig. S1c. The relative amounts of hydrocarbon species [34-37], including CH and C_2 species, increases with the CH_4% in gas mixture. The main phase and quality of diamond films after BEN pretreatment were analyzed by Raman spectrum in Fig. 2b. Optimized diamond growth is achieved at 20% CH_4 gas mixture as judged from the fingerprint diamond peak at 1332 cm^{-1} with a small FWHM (Full width at half maximum) value of ~ 25 in the Raman spectrum [8]. Using this condition, we grew a ~ 30 nm thick NCD film that is characterized by highly crystalline columnar grains, and the presence of an 1 nm thick amorphous carbon layer at the diamond/silicon interface (Fig. 2c-d and Fig. S1d-f).

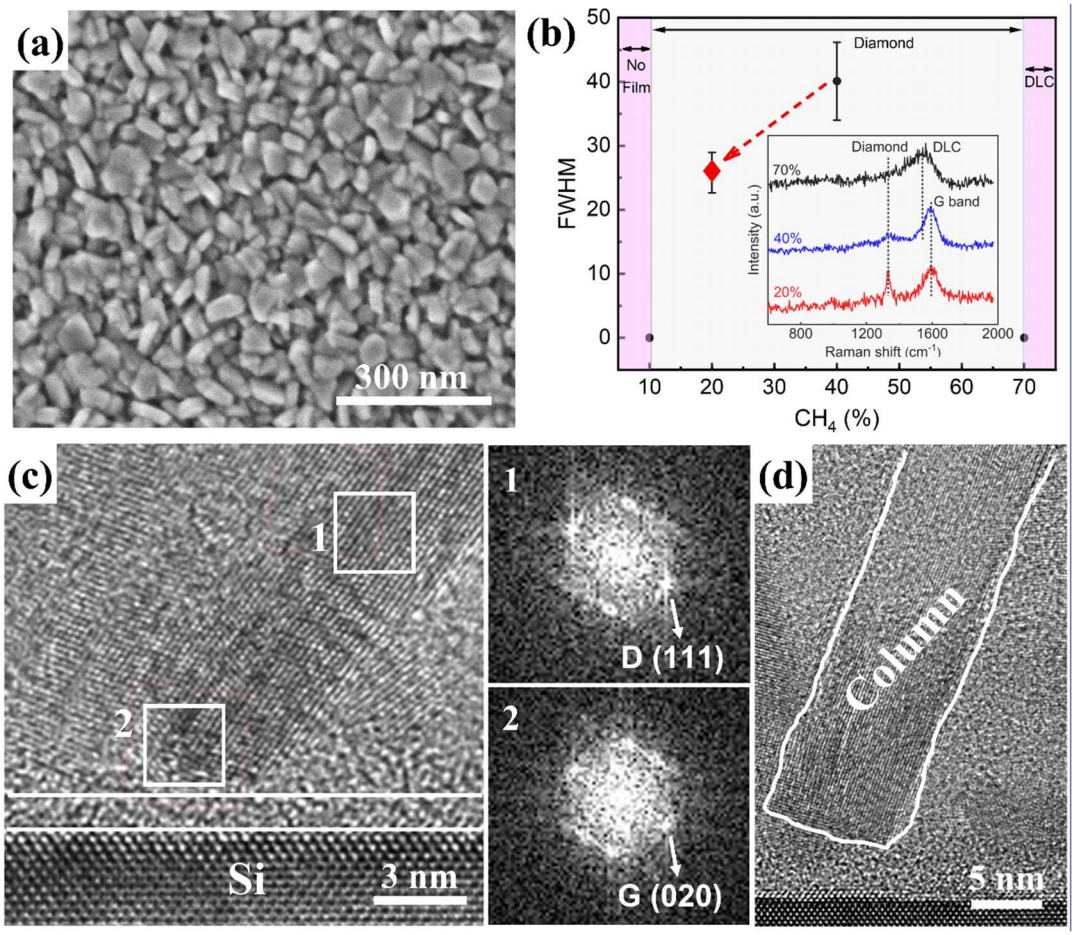

Fig. 2 Characterization of NCD film by BEN-assisted nucleation using $CH_4/H_2/CO_2$ gas mixture. **a** SEM image of as-grown diamond grains on silicon substrate in 20% CH_4 gas mixture. **b** Influence of various CH_4% gas mixture on the growth of NCD film. The insert shows the corresponding Raman spectrum of the film achieved at various CH_4% gases. **c-d** Cross sectional HRTEM images of the formed diamond grains in 20% CH_4 gas mixture. D and G in (c) represents diamond and graphite, respectively.

The evolution of optical properties of the NCD film with thickness was tracked by varying the deposition time. Prior to diamond film deposition, all the samples were pre-treated using the same BEN conditions in 20% CH_4 gas mixture for 30 min. The optical constants of diamond film, including refractive index n and extinction coefficient k, were presented in Fig. 3a. The refractive index gradually increases with diamond film thickness and approaches the value of bulk single crystal diamond (2.42 @ 632 nm) when film thickness reaches 500 nm. The extinction coefficient of the thick diamond film ($\geq$ 190 nm) approaches zero for wavelength above 400 nm, which

reflects the good transparency of diamond film. The change of optical constants should be attributed to the increase of sp^3-hybridized phase and structural variation as film thickness increases [38-40]. As shown in Fig. 3b, the calculated I_D/I_G ratio [41, 42] increases with diamond film thickness, demonstrating a reduction of the sp^2 hybridization carbon in the sp^3-hybridized carbon matrix as film gets thicker.

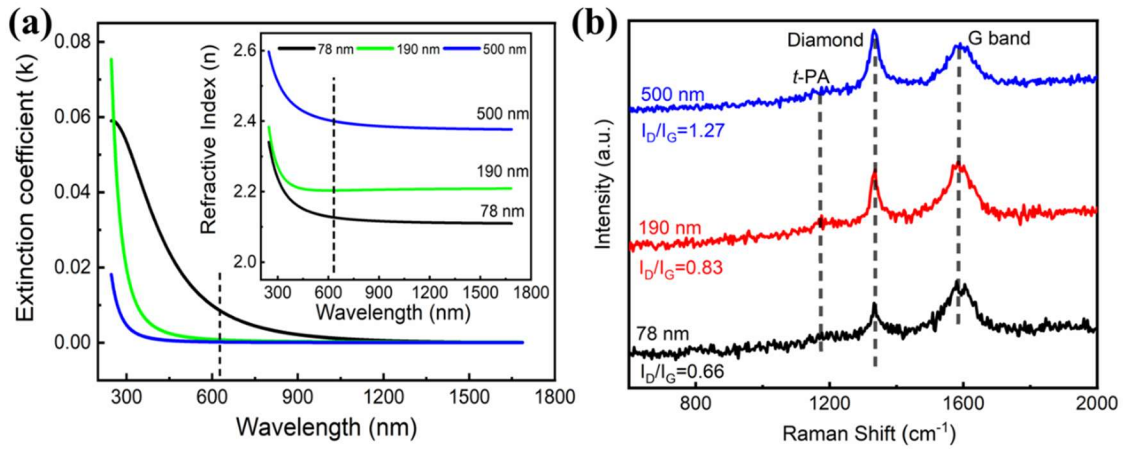

Fig. 3 Evolution of the optical properties with diamond film thickness. **a** Spectral dependence of diamond film as a function of film thickness. The insert in (a) shows the refractive index (n) curve of diamond film. **b** Raman spectrum of diamond film with different thickness. The I_D and I_G represents for the peak intensity of diamond and graphite phase respectively. The *t*-PA in (b) indicates trans-polyacetylene.

To extend the color gamut and demonstrate the feasibility of diamond metasurface for coloration, the symmetric cuboid with varying side length L $(L = L_x = L_y)$ and gap size g $(g = g_x = g_y)$ was developed on NCD/Si substrate by applying EBL and inductively coupled plasma (ICP) etching techniques. As shown in Fig. S2a-d, the fabricated diamond cuboid unit exhibits sharp edge profiles and its periodic arrangement results in a multiple-colors palette, where the length of diamond cuboid was varied from 130 nm to 505 nm and the gap size changed from 160 nm to 385 nm. To realize the application of diamond metasurface in cryptographic information, the dynamic functionalities of diamond metasurface color was also investigated with the high-aspect ratio $(L_x/L_y \approx 3.1)$ asymmetric cuboid unit. As shown in Fig. 4a, the cuboid unit exhibits subwavelength dimensions with width $L_y = 110$ nm and length $L_x = 350$ nm and forms a periodic array with varying gap sizes. The asymmetric configuration of cuboid units enables polarization-dependent response,

resulting in dynamic colors without changing materials properties [43, 44]. As shown in Fig. 4b, colors switching occurs depending on the polarization state, which is revealed by the pixel color change from orange, brown and green to blue, olive and pink respectively when the polarization state of light was turned from X-polarization state (0°) to Y-polarization state (90°). These measured reflectance spectra are consistent with the simulated ones in Fig. S3. The electromagnetic field distribution was simulated in Fig. S4a-d. To further investigate the optical response on diamond cuboid array, the multipolar modes of scattering cross-sections were decomposed into electric dipole (ED), magnetic dipole (MD), electric quadrupole (EQ) and magnetic quadrupole (MQ) modes in Fig. S4e. The excited magnetic dipole response is stronger than the electronic dipole response at $\lambda \approx 680$ nm on diamond cuboid, indicating that the optical resonance is dominated by MD at this wavelength. The test for cryptographic nanoprints in the image "Dragon" was decoded by applying the above asymmetric cuboid unit under 0° and 90° polarized light. The top-view SEM image of the "Dragon" pattern was shown in Fig. 4c. The overall size of the image is 600×450 μm. The pixel size varies between 5×7 and 9×17 array of diamond cuboids to fit the whole image. As shown in Fig. 4d-e, the color impression uniformly distributes on each part of the "Dragon" image and color distinction is well preserved even as the dimension of cuboid unit decreases. The dynamically switched "Dragon" image appears under different polarized-angle lights. To a certain degree, it is an angle-insensitive color printing performance of diamond metasurface. The observed color remains the same when the tilt angle was controlled within 13° under X-polarization state (0°) light (Fig. S5). Theoretically, when the incident electric filed is decomposed into two orthogonal coordinates (vertical and horizontal), the wavelength and polarized-angle-dependent reflectance [43, 45], which are believed due to the superposition of vertical and horizontal responses, can be expressed as:

$$R(\theta,\lambda) = R_V(\lambda)\sin^2(\theta) + R_H(\lambda)\cos^2(\theta) \quad (1)$$

θ is the polarized angle. λ [nm] is the wavelength of light in space. $R_V(\lambda)$ and $R_H(\lambda)$ represents for reflection of the polarized light along vertical (90°) and horizontal (0°) axis respectively. Take the "Dragon tail" as an example, when the polarization switches from 0° to 90°, the resonance mode excited by the horizontally polarized light ($\lambda \approx 680$ nm) vanishes while the resonance mode gets dominated by the vertically polarized light at $\lambda \approx 550$ nm, leading to the color switch from brown (0°) to olive (90°).

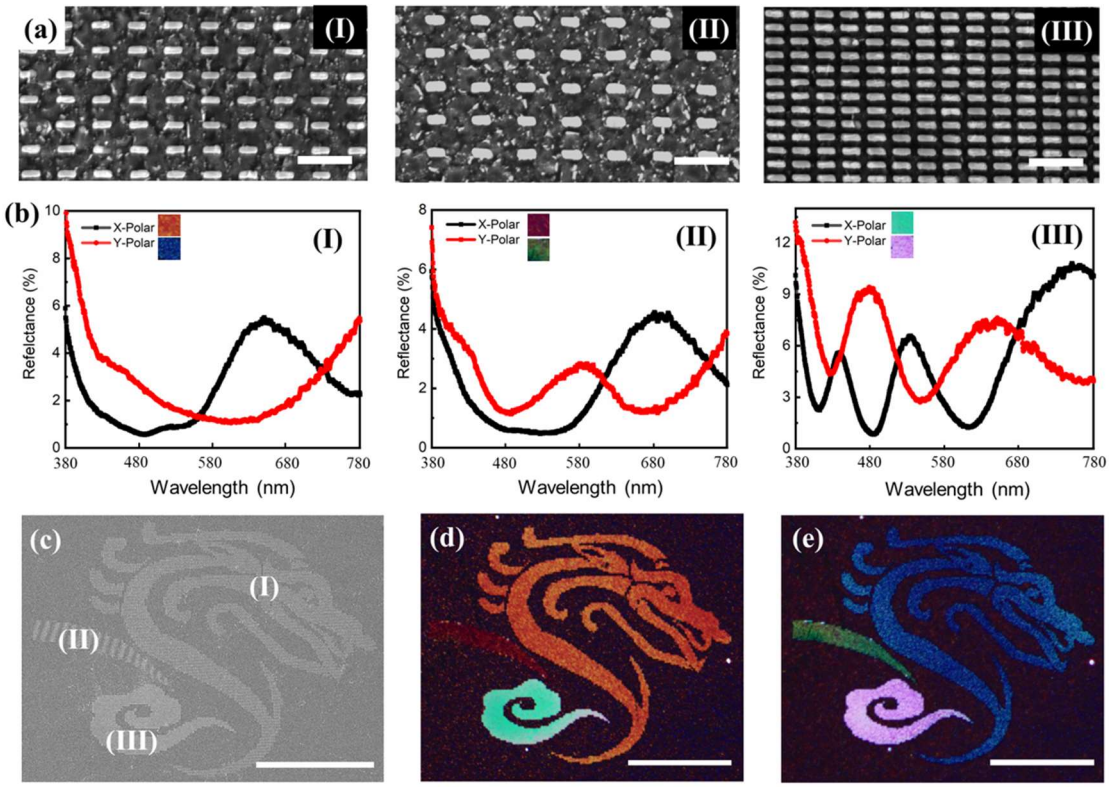

Fig. 4 Dynamic functions of diamond metasurface with structural colors. **a** SEM images of the designed asymmetric diamond cuboid periodically arranged with varying gap sizes. (I): $L_x = 350$ nm, $L_y = 110$ nm, $g_x = 340$ nm, $g_y = 320$ nm; (II): $L_x = 350$ nm, $L_y = 110$ nm, $g_x = 490$ nm, $g_y = 450$ nm; (III): $L_x = 350$ nm, $L_y = 110$ nm, $g_x = 120$ nm, $g_y = 150$ nm. The scale bar 1 μm. **b** The measured Reflectance spectra and corresponding colors under X- (0°) and Y- (90°) polarized light. **c** The top-view SEM image of the encrypted "Dragon" pattern. **d-e** The encrypted "Dragon" pattern was decoded by illumination under X- (0°) and Y- (90°) polarized light. The scale in (c-e) 200 um.

However, according to the results in Fig. S2d, the experimental reflectance spectra in CIE 1931 color map only occupy 22 % of the sRGB gamut and the corresponding coordinates distribute close to the center, indicating that the color performance suffers from low color saturation and small gamut. To solve the above problems, silicon substrate capped with a 70 nm Si_3N_4 layer was used to further suppress the reflection from substrate. A typical symmetric diamond cuboid array on $NCD/Si_3N_4/Si$ substrate is shown in Fig. S6. As shown in Fig. 5a-b, owing to the existence Si_3N_4 layer, the experimental multiple-colors palette shows higher color performance than that on NCD/Si substrate, which is evident from the improved color brightness, wide color gamut (65 % of the

sRGB) and much scattered coordinates of these measured reflectance spectra in CIE 1931 color map. The color performance strongly relies on the geometric size of diamond cuboid. As shown in Fig. 5c, the red shift of reflectance peak is observed with the change of pixel color when the cuboid length (L) increases from 280 nm to 505 nm at a constant 145 nm gap size. The well-matched results between measured and simulated reflectance confirm the better performance of these fabricated structural colors on $NCD/Si_3N_4/Si$ substrate (Fig. 5d). The intensity of measured reflectance peak reaches as high as ~ 28 % on array of symmetric diamond cuboid with length $L = 305$ at gap size 40 nm (Fig. S7). The influence of aspect-ratio of asymmetric diamond cuboid on coloration was investigated on $NCD/Si_3N_4/Si$ substrate in Fig. S8. Dynamic multiple-colors palette is obtained by solely varying the length L_y at constant $L_x = 360$ nm and obvious color-switch under X- (0°) and Y- (90°) polarized light is realized when the length $L_y \leq 160$ nm, demonstrating that the asymmetric diamond cuboid with high aspect ratio can enhance the function of dynamic coloration. However, the pixel color based on asymmetric diamond cuboid keeps constant when gap size becomes very large ($g > 310$ nm). It is widely believed that Mie scattering predominates when the grain dimension D fulfills the equation $\lambda/10 < D < \lambda$, where λ is the wavelength of incident light. Mie resonance occurs once the spatial dimension of nanostructure (L) is in the same scale as the wavelength of incident light ($L \approx \lambda/n$, n is the refractive index) [46-48]. For the diamond cuboid with dimension of $L = 280$ nm at $\lambda \approx 610$ nm, the condition of Mie resonance is well satisfied. The enhanced Mie resonance was further simulated on the asymmetric diamond cuboid array ($L = 280$ nm, $g = 145$ nm) in Fig. 5d-e. Two obvious resonances corresponding to electric dipole (ED) and magnetic dipole (MD), are clearly observed at $\lambda \approx 610$ nm. The excited magnetic dipole mode is stronger than the electric dipole mode due to the slightly higher refractive index of diamond cuboid [49].

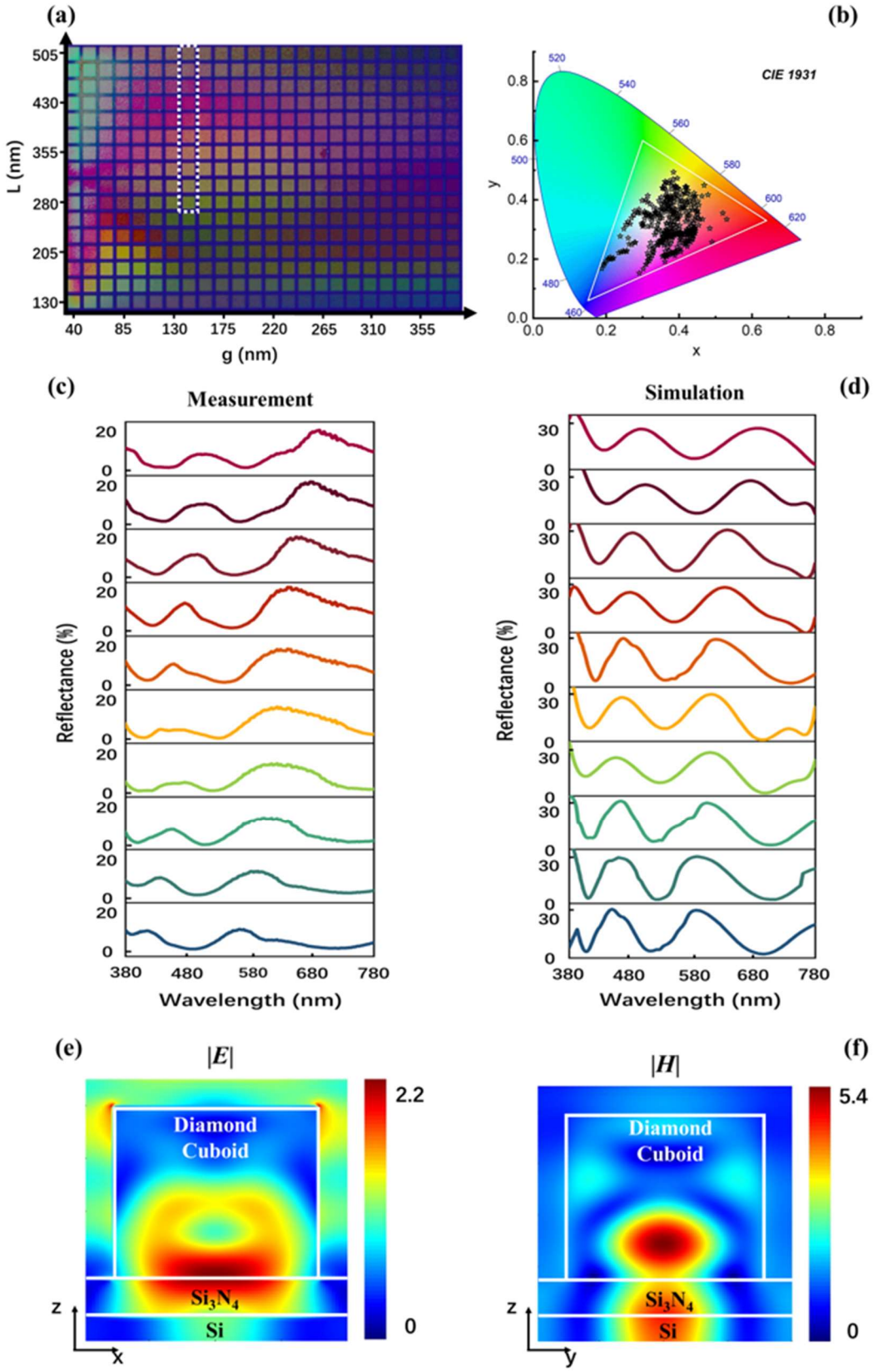

Fig. 5 Characterization and simulation analysis of structural colors produced by symmetric diamond cuboid $(L_x = L_y)$ nanostructures on $NCD/Si_3N_4/Si$ substrate. **a** The bright-field optical image of the fabricated multiple-colors palette by simultaneously varying the gap g $(g = g_x = g_y)$ and

length L ($L = L_x = L_y$) of diamond cuboid. Each unit pixel has a size of $10\ \mu m \times 10\ \mu m$. **b** CIE xy chromaticity coordinates of the measured reflectance spectra of color palette according to the designed diamond metasurface. The standard Red Green Blue (sRGB) space is present by white triangle. **c** Measured and simulated reflectance spectra for diamond nanostructures indicated by dashed box in (a), where the length L varies from $280\ nm$ to $505\ nm$ at constant gap size $g = 145\ nm$. **d** Spatial distributions of the simulated electrical field magnitude ($|\boldsymbol{E}|$) and magnetic field magnitude ($|\boldsymbol{H}|$) for diamond nanostructures where the diamond cuboid with length $L = 280\ nm$ periodically arranged at gap $g = 145\ nm$.

Owing to the formation of polarization-dependent colors on asymmetric diamond cuboid nanostructures, diamond metasurface shows great potential in information encryption. Structural color based on diamond metasurface exhibits long-time durability even in harsh environments. The presence of the randomly distributed small bump on the etched region (Light spot in Fig. 4d-e) can serve as the physical unclonable function tag [50] and promote the function of visible scattering [51], leading to high security and convenient authentication for practical encryption. By applying angle-resolved polarized light sources, the encoded information can be verified with these dynamic images. In addition, by precise control of geometrical parameters such as length, width and gap size at nanoscale size, a multiple-colors palette based on diamond metasurface is experimentally realized. The structural color displays relatively high color saturation and broad gamut (~ 65 % of sRGB) on $NCD/Si_3N_4/Si$ substrate. The gamut of diamond metasurfaces achieved here greatly surpassed that of metallic metasurface (45 % of sRGB) [20] but is slightly lower than that of conventional Si metasurfaces (~ 75 % of sRGB) [8]. At this stage, there is still plenty of room to improve the color saturation by improving the refractive index and configuration of the diamond unit cell.

4 Conclusion

In summary, we have successfully demonstrated structural colors on diamond metasurface. By tuning the plasma chemistry of the BEN process and optimizing the film thickness during the growth stage a $500\ nm$-thick NCD film with refractive index and optical transparency approaching that of bulk single crystal diamond was successfully synthesized and used for fabricating nanostructured metasurfaces consisting of diamond cuboid unit. Structural colorization

was realized by tuning the length and gap sizes of the symmetric/asymmetric diamond cuboid unit. Asymmetric diamond cuboid array with a high aspect ratio (~ 3.1) enabled polarization-dependent response, producing dynamic colors with high resolution. By optimizing the configuration of diamond-metasurface system, the color performance was improved with high brightness and a relative wide gamut (~ 65 % of the sRGB). The durability and dynamic functionalities of diamond metasurface color could be potentially used in information encryption. However, further work is needed to improve the color saturation, such as improving the refractive index of diamond film and optimizing the structure of diamond metasurface.

Acknowledgements

The authors acknowledge the Applied Materials - NUS Advanced Materials Corporate Lab. This research was supported by the A*STAR, under its Applied Materials-NUS Advanced Materials Corporate Lab (IAF-ICP Ref no.I1801E0022). In addition, Z.D. would like to acknowledge the funding support from A*STAR AME IRG grant (Project No. A20E5c0093), A*STAR CDA grant (Project No. C210112019) and A*STAR MTC IRG grant (Project No. M21K2c0116).

Funding Open access funding provided by Shanghai Jiao Tong University

Open Access This article is licensed under a Creative Commons Attribution 4.0 International License, which permits use, sharing, adaptation, distribution and reproduction in any medium or format, as long as you give appropriate credit to the original author(s) and the source, provide a link to the Creative Commons licence, and indicate if changes were made. The images or other third party material in this article are included in the article's Creative Commons licence, unless indicated otherwise in a credit line to the material. If material is not included in the article's Creative Commons licence and your intended use is not permitted by statutory regulation or exceeds the permitted use, you will need to obtain permission directly from the copyright holder. To view a copy of this licence, visit http://creativecommons.org/licenses/by/4.0/.

Supplementary Information The online version contains supplementary material.

References

1. B. Yang, W. Liu, Z. Li, H. Cheng, D. Y. Choi, S. Chen, J. Tian. Ultrahighly saturated structural colors enhanced by multipolar-modulated metasurfaces. Nano Lett. **19**(7), 4221-4228 (2019). https://doi.org/10.1021/acs.nanolett.8b04923

2. Y. Gu, L. Zhang, J. K. W. Yang, S. P. Yeo, C.W. Qiu. Color generation via subwavelength plasmonic nanostructures. Nanoscale. **7**(15), 6409-6419 (2015). https://doi.org/10.1039/C5NR00578G

3. T. Xu, H. Shi, Y.-K. Wu, A. F. Kaplan, J. G. Ok, L. J. Guo. Structural colors: From plasmonic to carbon nanostructures. Small. **7**(22), 3128-3136 (2011). https://doi.org/10.1002/smll.201101068

4. X. Liu, Z. Huang, J. Zang. All-dielectric silicon nanoring metasurface for full-color printing. Nano Lett. **20**(12), 8739-8744 (2020). https://doi.org/10.1021/acs.nanolett.0c03596

5. Y. Chen, X. Duan, M. Matuschek, Y. Zhou, F. Neubrech, H. Duan, N. Liu. Dynamic color displays using stepwise cavity resonators. Nano Lett. **17**(9), 5555-5560 (2017). https://doi.org/10.1021/acs.nanolett.7b02336

6. M. Miyata, H. Hatada, J. Takahara. Full-color subwavelength printing with gap-plasmonic optical antennas. Nano Lett. **16**(5), 3166-3172 (2016). https://doi.org/10.1021/acs.nanolett.6b00500

7. A. S. Roberts, A. Pors, O. Albrektsen, S. I. Bozhevolnyi. Subwavelength plasmonic color printing protected for ambient use. Nano Lett. **14**(2), 783-787 (2014). https://doi.org/10.1021/nl404129n

8. M. Yang, S. Bai, Q. Xu, J. Li, T. Shimada, Q. Li, T. Goto, R. Tu, S. Zhang. Mechanical properties of high-crystalline diamond films grown via laser mpcvd. Diam. Relat. Mater. **109**, 108094 (2020). https://doi.org/10.1016/j.diamond.2020.108094

9. S. Jahani, Z. Jacob. All-dielectric metamaterials. Nat. Nanotechnol. **11**(1), 23-36 (2016). https://doi.org/10.1038/nnano.2015.304

10. D. Sell, J. Yang, S. Doshay, K. Zhang, J. A. Fan. Visible light metasurfaces based on single-crystal silicon. ACS Photonics. **3**(10), 1919-1925 (2016). https://doi.org/10.1021/acsphotonics.6b00436

11. Z. Dong, J. Ho, Y. F. Yu, Y. H. Fu, R. Paniagua Dominguez, S. Wang, A. I. Kuznetsov, J. K. W. Yang. Printing beyond srgb color gamut by mimicking silicon nanostructures in free-space. Nano Lett. **17**(12), 7620-7628 (2017). https://doi.org/10.1021/acs.nanolett.7b03613

12. Z. Dong, L. Jin, S. D. Rezaei, H. Wang, Y. Chen, F. Tjiptoharsono, J. Ho, S. Gorelik, R. J. H. Ng, Q. Ruan, C.W. Qiu, J. K. W. Yang. Schrödinger's red pixel by quasi-bound-states-in-the-continuum. Sci. Adv. **8**(8), 4512 https://doi.org/10.1126/sciadv.abm4512

13. Y. Wu, W. Yang, Y. Fan, Q. Song, S. Xiao. TiO_2 metasurfaces: From visible planar photonics to photochemistry. Sci. Adv. **5**(11), 0939 https://doi.org/10.1126/sciadv.aax0939

14. J. Zhu, J. Han, X. Han, S. Meng, A. Liu, X. He. Optical properties of amorphous diamond films evaluated by non-destructive spectroscopic ellipsometry. Opt. Mater. **28**(5), 473-479 (2006). https://doi.org/10.1016/j.optmat.2005.04.008

15. S. E. Coe, R. S. Sussmann. Optical, thermal and mechanical properties of cvd diamond. Diam. Relat. Mater. **9**(9), 1726-1729 (2000). https://doi.org/10.1016/S0925-9635(00)00298-3

16. M. P. Hiscocks, K. Ganesan, B. C. Gibson, S. T. Huntington, F. Ladouceur, S. Prawer. Diamond waveguides fabricated by reactive ion etching. Opt. Express. **16**(24), 19512-19519 (2008). https://doi.org/10.1364/OE.16.019512

17. B. A. Fairchild, P. Olivero, S. Rubanov, A. D. Greentree, F. Waldermann, R. A. Taylor, I. Walmsley, J. M. Smith, S. Huntington, B. C. Gibson, D. N. Jamieson, S. Prawer. Fabrication of

ultrathin single-crystal diamond membranes. Adv. Mater. **20**(24), 4793-4798 (2008). https://doi.org/10.1002/adma.200801460
18. J. Jing, Y. C. Yiu, C. Chen, D. Lei, L. Shao, Q. Wang, K. H. Li, N. Wong, Z. Chu. A data-mining-assisted design of structural colors on diamond metasurfaces. Adv. Photon. Res. **3**(3), 2100292 (2022). https://doi.org/10.1002/adpr.202100292
19. S. Sun, Z. Zhou, C. Zhang, Y. Gao, Z. Duan, S. Xiao, Q. Song. All-dielectric full-color printing with tio$_2$ metasurfaces. ACS Nano. **11**(5), 4445-4452 (2017). https://doi.org/10.1021/acsnano.7b00415
20. S. D. Rezaei, R. J. Hong Ng, Z. Dong, J. Ho, E. H. H. Koay, S. Ramakrishna, J. K. W. Yang. Wide-gamut plasmonic color palettes with constant subwavelength resolution. ACS Nano. **13**(3), 3580-3588 (2019). https://doi.org/10.1021/acsnano.9b00139
21. T. Izak, O. Babchenko, M. Varga, S. Potocky, A. Kromka. Low temperature diamond growth by linear antenna plasma cvd over large area. Phys. Status Solidi B. **249**(12), 2600-2603 (2012). https://doi.org/10.1002/pssb.201200103
22. Y. Z. Huang, S. C. Tseng, Y. H. Chen, H. Y. Tsai. The mechanisms of carbon nano-flake balls growth by laser ablation and microwave plasma chemical vapor deposition. Surf. Coat. Technol. **425**, 127668 (2021). https://doi.org/10.1016/j.surfcoat.2021.127668
23. Y. Wang, W. Wang, G. Shu, S. Fang, B. Dai, J. Zhu. Virtues of ir(100) substrate on diamond epitaxial growth: First-principle calculation and xps study. J. Cryst. Growth. **560-561**, 126047 (2021). https://doi.org/10.1016/j.jcrysgro.2021.126047
24. P. R. Riley, P. Joshi, N. Khosla, R. J. Narayan, J. Narayan. Formation of q-carbon with wafer scale integration. Carbon. **196**, 972-978 (2022). https://doi.org/10.1016/j.carbon.2022.06.003
25. C. Sun, W. J. Zhang, N. Wang, C. Y. Chan, I. Bello, C. S. Lee, S. T. Lee. Crystal morphology and phase purity of diamond crystallites during bias enhanced nucleation and initial growth stages. J. Appl. Phys. **88**(6), 3354-3360 (2000). https://doi.org/10.1063/1.1289071
26. Y. C. Chen, X. Y. Zhong, A. R. Konicek, D. S. Grierson, N. H. Tai, I. N. Lin, B. Kabius, J. M. Hiller, A. V. Sumant, R. W. Carpick, O. Auciello. Synthesis and characterization of smooth ultrananocrystalline diamond films via low pressure bias-enhanced nucleation and growth. Appl. Phys. Lett. **92**(13), 133113 (2008). https://doi.org/10.1063/1.2838303
27. J. J. Alcantar Peña, E. de Obaldia, J. Montes Gutierrez, K. Kang, M. J. Arellano Jimenez, J. E. Ortega Aguilar, G. P. Suchy, D. Berman Mendoza, R. Garcia, M. J. Yacaman, O. Auciello. Fundamentals towards large area synthesis of multifunctional ultrananocrystalline diamond films via large area hot filament chemical vapor deposition bias enhanced nucleation/bias enhanced growth for fabrication of broad range of multifunctional devices. Diam. Relat. Mater. **78**, 1-11 (2017). https://doi.org/10.1016/j.diamond.2017.07.004
28. K. Y. Teng, H. C. Chen, G. C. Tzeng, C. Y. Tang, H. F. Cheng, I. N. Lin. Bias-enhanced nucleation and growth processes for improving the electron field emission properties of diamond films. J. Appl. Phys. **111**(5), 053701 (2012). https://doi.org/10.1063/1.3687918
29. J. Gu, Z. Chen, R. Li, X. Zhao, C. Das, V. Sahmuganathan, J. Sudijono, M. Lin, K. P. Loh. Nanocrystalline diamond film grown by pulsed linear antenna microwave cvd. Diam. Relat. Mater. **119**, 108576 (2021). https://doi.org/10.1016/j.diamond.2021.108576
30. A. Kromka, O. Babchenko, T. Izak, K. Hruska, B. Rezek. Linear antenna microwave plasma cvd deposition of diamond films over large areas. Vacuum. **86**(6), 776-779 (2012). https://doi.org/10.1016/j.vacuum.2011.07.008

31. M. Sobaszek, Ł. Skowroński, R. Bogdanowicz, K. Siuzdak, A. Cirocka, P. Zięba, M. Gnyba, M. Naparty, Ł. Gołuński, P. Płotka. Optical and electrical properties of ultrathin transparent nanocrystalline boron-doped diamond electrodes. Opt. Mater. **42**, 24-34 (2015). https://doi.org/10.1016/j.optmat.2014.12.014
32. Z. G. Hu, P. Prunici, P. Hess, K. H. Chen. Optical properties of nanocrystalline diamond films from mid-infrared to ultraviolet using reflectometry and ellipsometry. J. Mater. Sci.: Mater. Electron. **18**(1), 37-41 (2007). https://doi.org/10.1007/s10854-007-9175-y
33. R. Bogdanowicz, M. Śmietana, M. Gnyba, J. Ryl, M. Gardas. Optical and structural properties of polycrystalline cvd diamond films grown on fused silica optical fibres pre-treated by high-power sonication seeding. Appl. Phys. A. **116**(4), 1927-1937 (2014). https://doi.org/10.1007/s00339-014-8355-x
34. Y. Yamamoto, S. Inoue, Y. Matsumura. Thermal decomposition products of various carbon sources in chemical vapor deposition synthesis of carbon nanotube. Diam. Relat. Mater. **75**, 1-5 (2017). https://doi.org/10.1016/j.diamond.2016.11.017
35. J. G. Buijnsters, L. Vázquez. Growth dynamics of nanocrystalline diamond thin films deposited by hot filament chemical vapor deposition: Influence of low sticking and renucleation processes. J. Phys. Chem. C. **115**(19), 9681-9691 (2011). https://doi.org/10.1021/jp201919r
36. A. P. Bolshakov, V. G. Ralchenko, G. Shu, B. Dai, V. Y. Yurov, E. V. Bushuev, A. A. Khomich, A. S. Altakhov, E. E. Ashkinazi, I. A. Antonova, A. V. Vlasov, V. V. Voronov, Y. Y. Sizov, S. K. Vartapetov, V. I. Konov, J. Zhu. Single crystal diamond growth by mpcvd at subatmospheric pressures. Mater. Today Commun. **25**, 101635 (2020). https://doi.org/10.1016/j.mtcomm.2020.101635
37. A. P. Bolshakov, V. G. Ralchenko, V. Y. Yurov, A. F. Popovich, I. A. Antonova, A. A. Khomich, E. E. Ashkinazi, S. G. Ryzhkov, A. V. Vlasov, A. V. Khomich. High-rate growth of single crystal diamond in microwave plasma in CH_4/H_2 and $CH_4/H_2/Ar$ gas mixtures in presence of intensive soot formation. Diam. Relat. Mater. **62**, 49-57 (2016). https://doi.org/10.1016/j.diamond.2015.12.001
38. J. Robertson. Diamond-like amorphous carbon. Mater. Sci. Eng. R Rep. **37**(4), 129-281 (2002). https://doi.org/10.1016/S0927-796X(02)00005-0
39. M. Ficek, K. J. Sankaran, J. Ryl, R. Bogdanowicz, I. N. Lin, K. Haenen, K. Darowicki. Ellipsometric investigation of nitrogen doped diamond thin films grown in microwave $ch_4/h_2/n_2$ plasma enhanced chemical vapor deposition. Appl. Phys. Lett. **108**(24), 241906 (2016). https://doi.org/10.1063/1.4953779
40. O. A. Williams, M. Nesládek. Growth and properties of nanocrystalline diamond films. Phys.Status. Solidi. **203**(13), 3375-3386 (2006). https://doi.org/10.1002/pssa.200671406
41. A. K. C, R. Saha, J. Anderson, A. Ayala, C. Engdahl, E. L. Piner, M. W. Holtz. Effect of seeding density on the growth of diamond films by hot-filament chemical vapor deposition from sparse to dense range. J. Appl. Phys. **130**(22), 225302 (2021). https://doi.org/10.1063/5.0068541
42. B. Paramanik, D. Das. Synthesis of nanocrystalline diamond embedded diamond-like carbon films on untreated glass substrates at low temperature using (C_2H_2+H_2) gas composition in microwave plasma cvd. Appl. Surf. Sci. **579**(152132 (2022). https://doi.org/https://doi.org/10.1016/j.apsusc.2021.152132
43. J. Jang, H. Jeong, G. Hu, C. W. Qiu, K. T. Nam, J. Rho. Kerker-conditioned dynamic cryptographic nanoprints. Adv. Opt. Mater. **7**(4), 1801070 (2019). https://doi.org/10.1002/adom.201801070

44. C. Matricardi, J. L. Garcia Pomar, P. Molet, L. A. Pérez, M. I. Alonso, M. Campoy Quiles, A. Mihi. High-throughput nanofabrication of metasurfaces with polarization-dependent response. Adv. Opt. Mater. **8**(20), 2000786 (2020). https://doi.org/10.1002/adom.202000786
45. T. Ellenbogen, K. Seo, K. B. Crozier. Chromatic plasmonic polarizers for active visible color filtering and polarimetry. Nano Lett. **12**(2), 1026-1031 (2012). https://doi.org/10.1021/nl204257g
46. Y. Kivshar. The rise of mie-tronics. Nano Lett. **22**(9), 3513-3515 (2022). https://doi.org/10.1021/acs.nanolett.2c00548
47. Y. Kivshar, A. Miroshnichenko. Meta-optics with mie resonances. Opt. Photon. News. **28**(1), 24-31 (2017). https://doi.org/10.1364/OPN.28.1.000024
48. M. L. De Marco, S. Semlali, B. A. Korgel, P. Barois, G. L. Drisko, C. Aymonier. Silicon-based dielectric metamaterials: Focus on the current synthetic challenges. Angew. Chem. Int. Ed. **57**(17), 4478-4498 (2018). https://doi.org/https://doi.org/10.1002/anie.201709044
49. A. I. Kuznetsov, A. E. Miroshnichenko, M. L. Brongersma, Y. S. Kivshar, B. Luk'yanchuk. Optically resonant dielectric nanostructures. Science. **354**(6314), aag2472 (2016). https://doi.org/10.1126/science.aag2472
50. Y. Fan, C. Zhang, Z. Gao, W. Zhou, Y. Hou, Z. Zhou, J. Yao, Y. S. Zhao. Randomly induced phase transformation in silk protein-based microlaser arrays for anticounterfeiting. Adv. Mater. **33**(42), 2102586 (2021). https://doi.org/10.1002/adma.202102586
51. Z. Xu, H. Luo, H. Zhu, Y. Hong, W. Shen, J. Ding, S. Kaur, P. Ghosh, M. Qiu, Q. Li. Nonvolatile optically reconfigurable radiative metasurface with visible tunability for anticounterfeiting. Nano Lett. **21**(12), 5269-5276 (2021). https://doi.org/10.1021/acs.nanolett.1c01396